

This is an Open Access document downloaded from ORCA, Cardiff University's institutional repository: <https://orca.cardiff.ac.uk/id/eprint/129518/>

This is the author's version of a work that was submitted to / accepted for publication.

Citation for final published version:

Hong, John, Lee, Young-Woo, Hou, Bo , Ko, Wonbae, Lee, Juwon, Pak, Sangyeon, Hong, JinPyo, Morris, Stephen M., Cha, SeungNam, Sohn, Jung Inn and Kim, Jong Min 2016. Solubility-dependent NiMoO₄ nanoarchitectures: direct correlation between rationally designed structure and electrochemical pseudokinetics. *ACS Applied Materials and Interfaces* 8 (51) , pp. 35227-35234. 10.1021/acsami.6b11584

Publishers page: <http://dx.doi.org/10.1021/acsami.6b11584>

Please note:

Changes made as a result of publishing processes such as copy-editing, formatting and page numbers may not be reflected in this version. For the definitive version of this publication, please refer to the published source. You are advised to consult the publisher's version if you wish to cite this paper.

This version is being made available in accordance with publisher policies. See <http://orca.cf.ac.uk/policies.html> for usage policies. Copyright and moral rights for publications made available in ORCA are retained by the copyright holders.



1
2
3
4 **Solubility-dependent NiMoO₄ nanoarchitectures: Direct correlation between rationally**
5
6 **designed structure and electrochemical pseudo-kinetics**
7
8
9

10
11 John Hong^a, Young-Woo Lee^a, Bo Hou^a, Wonbae Ko^b, Juwon Lee^a, Sangyeon Pak^a,

12
13
14 JinPyo Hong^b, Stephen M. Morris^a, SeungNam Cha^{a,*}, Jung Inn Sohn^{a,*} and Jong Min Kim^c
15
16
17
18
19
20
21
22

23 ^a Department of Engineering Science, University of Oxford, Parks Road, Oxford, OX1 3PJ, United
24 Kingdom.
25

26
27 ^b Research Institute of Convergence of Basic Science, Novel Functional Materials and Device
28 Laboratory, Department of Physics, Hanyang University, Seoul 133-791, Korea.
29

30
31 ^c Electrical Engineering Division, Department of Engineering, University of Cambridge, 9 JJ
32 Thomson Avenue, Cambridge, CB3 0FA, United Kingdom.
33
34
35
36
37
38
39
40
41
42
43
44
45
46
47
48
49
50
51
52
53
54
55

56 * Corresponding author. Tel: +44-1865-273912. Fax: +44-1865-273010.

57
58 E-mail address: seungnam.cha@eng.ox.ac.uk; junginn.sohn@eng.ox.ac.uk.
59
60

1
2
3
4 **Abstract**
5

6 Pseudocapacitors have recently attracted attention from the scientific community as a
7 promising new energy storage system, which can potentially bridge the performance gap
8 between lithium ion batteries and conventional capacitors. To further improve the
9 performance of these pseudocapacitors, tailoring the binary metal oxide along with
10 developing new methods for controlling resultant nanostructures in a predictive way is an
11 essential requirement for achieving more favorable electrochemical kinetics. Here, through a
12 simple hydrothermal synthetic procedure that uses different supersaturation states to alter the
13 driving force for crystal growth, we have managed to obtain one-dimensional (1-D) Nickel
14 Molybdenum Oxide (NiMoO₄) electrodes on a nickel foam. The morphology of the 1-D
15 NiMoO₄ nanostructures can be tuned from a low to a high aspect ratio (over a range of
16 diameter sizes from 80 to 800 nm). Such a controllable structure provides a platform for
17 understanding the electrochemical relationships in terms of fast retention times and improved
18 ion diffusion coefficients, enabling the demonstration of promising electrochemical storage
19 properties. We show that the 1-D NiMoO₄ electrode with a high aspect ratio (HAR) exhibits a
20 much higher specific capacitance of 1335 F g⁻¹ at a current density of 1 A g⁻¹, which is due to
21 the unique physical and chemical structure being suitable for electrochemical kinetics. We
22 further demonstrate that an asymmetric supercapacitor consisting of the tailored HAR-
23 NiMoO₄ electrode can achieve an energy density of 40.7 Wh kg⁻¹ and a power density of 16
24 kW kg⁻¹.
25
26
27
28
29
30
31
32
33
34
35
36
37
38
39
40
41
42
43
44
45
46
47
48
49
50
51
52
53
54

55 **Keywords:** Energy storage material, Electrochemical reaction kinetics, Nanowire architecture,
56 Controlled aspect ratio, Asymmetric supercapacitor
57
58
59
60

1. INTRODUCTION

Electrochemical supercapacitors are currently being considered as promising candidates for next-generation energy storage applications since they have the potential to bridge the gap between batteries and conventional capacitors for the production of high power and high energy densities. Furthermore, they have been shown to exhibit a good rate capability, long cycling life time, and environmentally friendly characteristics.¹⁻³ In particular, pseudocapacitors, which possess the capability to store large amounts of charge *via* fast and reversible electrochemical Faradaic redox reactions, have enormous potential in a broad variety of applications, including electric vehicles and portable electronic devices.^{4,5} Currently, transition metal oxides/hydroxides such as RuO₂, Ni(OH)₂, Co₃O₄ and MnO₂, are most commonly used as the electrode materials with high theoretical capacitances because of their multiple oxidation states, enabling rich electrochemical Faradaic reactions.⁶⁻⁹

Despite their compelling benefits combined with the inherently high electrochemical activities, their low conductivity and structural instability, which leads to a reduction in the performance, continuously hinders the successful exploitation of pseudocapacitor technology in practical applications.¹⁰ To overcome these limitations, numerous studies have been devoted to enhancing the electrochemical properties of the pseudocapacitors by focusing on the development of new electrode materials that are based on binary transition metal oxides.¹¹⁻¹⁴ These materials typically exhibit a higher electrical conductivity and richer chemical valence states than the single-component transition metal oxides, which arises from the combined contributions from both metal atoms.¹¹⁻¹⁴ Among the various binary metal oxides, transition metal molybdates such as NiMoO₄ and CoMoO₄ are an emerging class of pseudocapacitor materials that have received considerable attention due to their cost-effectiveness, abundance, and chemical stability.^{15,16} More specifically, the primary interest in NiMoO₄ lies in the fact that the high specific capacitance from the Ni atom and the high

1
2
3
4 electrical conductivity from the Mo atom can contribute collectively to the superior
5
6 electrochemical behavior when used in energy storage devices.¹⁷ Combined, these features
7
8 demonstrate that NiMoO₄ has potential in future pseudocapacitor energy storage systems.
9

10
11 Alternatively, various nanostructuring approaches have been developed to address
12
13 issues related to limited electrochemical kinetics on the surface, which are strongly associated
14
15 with a low degree of surface contact areas and low ion diffusion rates.¹⁸⁻¹⁹ These more recent
16
17 strategies have shown that hierarchical nanostructures with diverse morphologies and
18
19 dimensions (D) can provide more active sites and shorter ion diffusion pathways, which then
20
21 stimulate and facilitate the kinetics associated with the electrochemical reactions. In
22
23 particular, 1-D nanostructures are one of the most widely used architectures for
24
25 electrochemical storage devices mainly because 1) the unique geometry results in a large
26
27 contact surface area; 2) the structures exhibit short diffusion distance; 3) they exhibit good
28
29 structural stability and 4) they possess a favorable charge carrier path during the
30
31 charge/discharge processes. Nevertheless, synthesizing these 1-D structures in binary metal
32
33 oxides in a controlled way still remains a challenge and is mainly due to the complex
34
35 stoichiometry-dependent synthetic reactions. Further, even though there have been few
36
37 reports²⁰⁻²¹ that have studied the dependence of the electrochemical storage performance on
38
39 the different nanostructures, there are no detailed studies that directly describe the
40
41 electrochemical ion intercalation mechanism for engineering 1-D nanostructures with tailored
42
43 aspect ratios.
44
45
46

47
48 It is, therefore, highly desirable that a novel and facile synthetic route for the
49
50 preparation of 1-D nanostructured binary metal oxides with different aspect ratios be
51
52 developed that can enhance the charge transfer kinetics so as to improve charge
53
54 transportation. Moreover, developing such a procedure would enable us to understand how
55
56 the charge storage dynamics and electrochemical stability depends upon the nanostructure
57
58
59
60

1
2
3
4 and how this can lead to a superior pseudocapacitor performance. To this end, we have
5
6 employed the fundamental principle of hydrothermal reaction kinetics whereby the nucleation
7
8 and crystallization growth rates can depend crucially on the supersaturation states of the
9
10 solvents, which are the major driving forces for solution-based synthetic processes as shown
11
12 in Figures 1a-c.²² Controlling the rational supersaturated environments enables the synthesis
13
14 of 1-D NiMoO₄ nanostructures with different, but predictable, morphologies. In this regard,
15
16 we propose a simple and facile way for the rational and precise design of the desirable
17
18 supersaturation levels, which in turn affects the crystal nucleation rates and preferred crystal
19
20 growth geometries and directions thereby leading to different 1-D aspect ratios. Moreover,
21
22 the different 1-D NiMoO₄ nanostructures can result in a diverse range of electrochemical
23
24 behavior including specific capacitance as well as ion diffusion and charge transfer dynamics.
25
26 Through the control of these properties, it therefore provides one of the best routes for the
27
28 design of new electrode materials for high-performance supercapacitors.
29
30
31
32
33
34

35 **2. EXPERIMENTAL DETAILS**

36 **2.1 Material synthesis: NiMoO₄ nanostructures on a Ni foam.**

37
38
39
40 Different 1-D NiMoO₄ nanostructures with different aspect ratios on nickel foams
41
42 were synthesized by a hydrothermal method. First, a conductive Ni foam (1 cm x 1 cm) was
43
44 cleaned using 1 M HCl, ethanol, and deionized water. In a typical synthesis, 1.0 mmol of
45
46 Ni(NO₃)₂·6H₂O and 1.0 mmol of Na₂MoO₄ were dissolved in deionized water at room
47
48 temperature to form a clear green solution. After being stirred for an hour, the solution was
49
50 transferred into a 45 ml Teflon-lined cup, and then the Ni foam was transferred into the
51
52 Teflon-lined cup and a stainless steel autoclave. The hydrothermal reaction was carried out at
53
54 140 °C for 4 hr. After cooling down naturally to room temperature, the Ni foam was collected
55
56 and washed several times with water and ethanol to remove loosely attached NiMoO₄ on the
57
58
59
60

1
2
3
4 Ni foam. The foam was then fully dried at 60 °C for 12 hr. In order to obtain the crystallized
5
6 NiMoO₄ nanostructures, the Ni foam with the NiMoO₄ nanostructure was calcined at 400 °C
7
8 for 2 hr in an argon atmosphere. The different nanostructures of the NiMoO₄ material were
9
10 synthesized using various solvents with different mixtures of solvents such as water, ethanol
11
12 and hydrochloric acids.
13

14 **2.2 Material characterization**

15
16 Morphologies of the samples were characterized by SEM (Hitachi S-4300) and TEM
17
18 (JEOL JEM-2200MCO FEGTEM). The crystal structure of the samples was examined by
19
20 high resolution XRD (Rigaku Medel Smartlab) in a two theta range of 10-80°. The specific
21
22 BET surface area was calculated on the basis of nitrogen adsorption isotherms using
23
24 Micromeritics Gemini VI. XPS were recorded using a Thermo Scientific K-Alpha XPS
25
26 instrument equipped with a micro-focused mono-chromated Al X-ray source. The XPS
27
28 source was operated at 12 keV and a 400 μm spot size was used. The spectrometer was
29
30 adjusted to align a binding energy of 284.5eV for the C 1s line.
31
32
33

34 **2.3 Electrochemical characterization**

35
36 The electrochemical properties of the NiMoO₄ samples with different aspect ratios
37
38 were measured in a three-electrode system consisting of HAR-, MAR-, and LAR-NiMoO₄
39
40 electrodes as working electrodes, Pt mesh as a counter electrode, and an Ag/AgCl electrode
41
42 (in saturated 3 M KCl) as a reference electrode. These were used to analyze CV, galvanostatic
43
44 charge/discharge, and EIS curves using a potentiostat (PGSTAT302N, Metrohm, Autolab).
45
46 For the fabrication of the anode electrodes, active carbon was prepared as an active material,
47
48 with poly(vinylidene difluoride) as a binder and Ketjen black as a conductive material, and
49
50 this was then coated onto the compressed nickel foam as a current collector. All
51
52 electrochemical results of the AC//HAR-NiMoO₄ ASC were measured using a two electrode
53
54 system under 1.0 M KOH solution at room temperature.
55
56
57
58
59
60

3. RESULTS AND DISCUSSION

The morphology and structural characteristics of the as-prepared NiMoO₄ materials were investigated by scanning electron microscopy (SEM). As shown in Figures 1d-f, the controlled growth of the 1-D NiMoO₄ nanostructures with different aspect ratios was successfully achieved on a nickel foam through a hydrothermal process by adjusting the solubility level in the reaction solution and hence introducing various different supersaturation states during the growth phase. Obviously, as the relative solubility decreases, the morphology of the 1-D nanostructures is transformed through a series of distinct aspect ratios between length to breadth from a low (LAR) to a high value (HAR) through a medium value (MAR). Figure 1d shows an SEM image of the MAR-NiMoO₄ sample obtained from the DI water-only solution, which results in 1-D nanostructures with a diameter size of ~250 nm. In contrast, the HAR-NiMoO₄ sample with a diameter of about 80 nm is grown under low solubility conditions induced by adding an alkaline solvent into the water solution (Figure 1d). Finally, the LAR-NiMoO₄ sample has a diameter of 800 nm and was constructed by introducing an additional acidic solvent (Figure 1f). These findings indicate that introducing a low (high) solubility environment to the hydrothermal precursor solution induces the relatively high (low) degree of supersaturation, leading to a higher (lower) driving force for crystal nucleation and growth process. Therefore, the selective synthesis mechanism responsible for the different 1-D NiMoO₄ structures can be understood in terms of the control of the solvent solubility that leads to different degrees of supersaturation. Moreover, a predictable 1-D nanostructure synthetic route so as to grow the active materials directly on to a metal collector means that the driving force for nucleation and crystal growth can be controlled by changing the supersaturation states.

Next, the nanostructures of the HAR-, MAR- and LAR-NiMoO₄ samples were

1
2
3
4 further characterized by transmission electron microscopy (TEM) to provide more insight
5
6 regarding their unique 1-D structure, as shown in inset images of Figures 1d-f. The TEM
7
8 images clearly demonstrate that the diameter of 1-D nanostructures for the as-prepared
9
10 NiMoO₄ samples is in good agreement with the SEM results. As a result of tuning the
11
12 solubility of the solvents, three different types of 1-D NiMoO₄ material with mean aspect
13
14 ratios of 21.6 (HAR-NiMoO₄), 12.8 (MAR-NiMoO₄), and 4.7 (LAR-NiMoO₄) were
15
16 successfully prepared for use in a supercapacitor application (Supporting Information Figure
17
18
19 S1).

20
21
22 To evaluate the crystallographic phase of the NiMoO₄ electrode samples, X-ray
23
24 diffraction (XRD) spectra were analyzed, which are shown in Figure 2a. All the diffraction
25
26 patterns obtained from the 1-D NiMoO₄ nanostructures with different aspect ratios are
27
28 unambiguously assigned to the NiMoO₄ phase (JCPDS Card No. 86-0361) without any
29
30 noticeable differences.²³ Moreover, to confirm the surface electronic states and chemical
31
32 compositions of the NiMoO₄ samples, X-ray photoelectron spectroscopy (XPS)
33
34 measurements were carried out. Figures 2c-d compare the high resolution XPS spectra of the
35
36 Ni 2p and Mo 3d of the 1-D NiMoO₄ samples with different aspect ratios, respectively. The
37
38 Ni 2p doublet is clearly observed at 854.9 eV (Ni²⁺ 2p_{3/2}) and at 872.5 eV (Ni²⁺ 2p_{1/2}) with a p
39
40 spin-orbit splitting of 17.6 eV.²⁴ Moreover, the two peaks at binding energies of 232.0 eV and
41
42 235.1 eV with the d spin-orbit splitting of 3.1 eV correspond to Mo⁶⁺ 3d_{5/2} and Mo⁶⁺ 3d_{3/2},
43
44 respectively.²⁵ These XPS results suggest that there are only chemical oxidation states and
45
46 compositions of the Ni²⁺ and Mo⁶⁺ in the as-prepared 1-D NiMoO₄ whereby the Ni cations,
47
48 distributed in octahedral sites, are electrochemically active with OH⁻ electrolyte ions and the
49
50 Mo cations in tetrahedral sites contribute to the electrochemical stability.

51
52
53 To further examine the specific surface area characteristics of the 1-D NiMoO₄
54
55 structures, measurements of the N₂ adsorption-desorption were carried out (Supporting
56
57
58
59
60

1
2
3
4 Information Figure S2). As shown in Figure 2b, the calculated Brunauer-Emmett-Teller
5 (BET) surface area of the HAR-NiMoO₄ sample has the largest value (97.26 m² g⁻¹) and is
6 much larger than the areas for the MAR-NiMoO₄ (50.32 m² g⁻¹) and LAR-NiMoO₄ (25.66 m²
7 g⁻¹) samples, which is mainly due to the different aspect ratios of the nanostructures. This
8 implies that the high surface area of the HAR-NiMoO₄ electrodes provides a sufficient
9 electrolyte contact interface and can thus enhance the kinetics of ion diffusion. Consequently,
10 a high aspect ratio can improve the electrochemical capacitance and the charge transfer
11 kinetics.
12
13
14
15
16
17
18
19
20
21

22 In order to evaluate the electrochemical performance of the different 1-D
23 morphologies, the HAR-, MAR- and LAR-NiMoO₄ were applied directly as working
24 electrodes in a three electrode system. Supporting Information Figure S3 shows the cyclic
25 voltammetry (CV) and the galvanostatic charge-discharge curves of the each NiMoO₄
26 electrode. First, the CV curves of all the NiMoO₄ electrodes have similar shapes with
27 increasing scan rates, indicating that all the electrodes have good pseudocapacitive
28 behavior.²⁶ For a direct CV performance comparison between the electrodes, Figure 3a
29 presents the CV curves of the three different types of NiMoO₄ electrodes with the potential
30 window ranging from 0.0 to 0.6 V at a scan rate of 5 mV s⁻¹. It can be clearly observed that
31 all the NiMoO₄ electrodes have a couple of Faradaic reaction peaks that can be ascribed to
32 the reversible redox reaction between Ni(II) and Ni(III).²⁷ The area surrounded within the CV
33 curve of the HAR-NiMoO₄ sample occupies the largest area, indicating the highest value for
34 the electrochemical capacitance. This large CV area might be attributed to the larger
35 electrolyte contact area for the HAR-NiMoO₄ electrode. Consistent with the CV results, the
36 galvanostatic charge-discharge curves demonstrate that the HAR-NiMoO₄ electrode has the
37 longest discharge time (Supporting Information Figure S3). Moreover, the calculated specific
38 capacitance of the HAR-, MAR-, and LAR-NiMoO₄ samples at a current density of 1 A g⁻¹
39
40
41
42
43
44
45
46
47
48
49
50
51
52
53
54
55
56
57
58
59
60

1
2
3
4 are 1335 F g⁻¹, 1106 F g⁻¹ and 672 F g⁻¹, respectively (Supporting Information Figure S4).
5

6
7 In order to better understand the ion diffusion behavior and charge transfer dynamics
8 of the NiMoO₄ electrodes with tailored aspect ratios, kinetic electrochemical analysis was
9 carried out. The inset of Figure 3a indicates the potential difference of each electrode between
10 the anodic and cathodic peak, representing the degree of reversible intercalation and de-
11 intercalation dynamics during the CV charge-discharge.²⁸ It can be seen that the HAR-
12 NiMoO₄ electrode provides a much more appreciable OH⁻ ion access and faster charge
13 transfer rate. Moreover, the cathodic peak current densities of the NiMoO₄ electrodes were
14 plotted as a function of the square root of the scan rates in Figure 3b. The cathodic peak
15 currents increase linearly, showing that redox reactions at the surface are followed by a
16 diffusion-controlled process with the OH⁻ ions.²⁹ Also, it is evident that the cathodic peak
17 current of the HAR-NiMoO₄ sample shows a steeper dependence compared to the other
18 electrodes, indicating a larger diffusion coefficient. For a direct comparison of the ion
19 diffusivity, the diffusion coefficients of the NiMoO₄ electrodes were calculated according to
20 the following Randles–Sevcik equation.³⁰
21
22
23
24
25
26
27
28
29
30
31
32
33
34
35
36

$$i_p = (2.69 * 10^5) * n^{\frac{3}{2}} * A * D_0^{\frac{1}{2}} * C_0 * v^{\frac{1}{2}}$$

37
38
39
40
41 where i_p is the cathodic peak current density, n is the number of electrons, A is the electrode
42 area, D_0 is the diffusion coefficient, C_0 is the electrolyte concentration, and v is the scan rate.
43 We can assume that n , A , C_0 have the same values in the same three electrode system.
44 Therefore, the diffusion coefficient of the 1-D NiMoO₄ samples can be directly compared
45 from the slope of the curve ($D_0^{\frac{1}{2}} \propto i_p/v^{\frac{1}{2}}$). The diffusion coefficient of the HAR-NiMoO₄ sample
46 is found to be 1.82 and 17.9 times larger than that of the MAR- and LAR-NiMoO₄ samples,
47 respectively.
48

49
50
51
52
53
54
55
56
57
58 Figure 3c presents the specific rate retention data as a function of the current density

59
60
1
2
3
4 in the electrodes. From a low current density of 1 A g⁻¹ to a high current density of 20 A g⁻¹,
5
6 the capacitance of the HAR-NiMoO₄ electrode shows good rate retention behavior, which is
7
8 found to be 882.4 F g⁻¹ at 20 A g⁻¹ with ~ 66.1 % retention compared to that for 1 A g⁻¹. On the
9
10 other hand, for the MAR and LAR-NiMoO₄ electrodes the capacitance is recorded to be
11
12 668.8 F g⁻¹ and 146.0 F g⁻¹ with 60.5 % and 21.8 % rate retention, respectively. In other
13
14 words, the presence of the fast diffusion rate from the surface to the internal structure means
15
16 that the HAR-NiMoO₄ electrode exhibits much better retention performance.
17

18
19
20 Finally, to elucidate further the ion diffusion and charge transfer behavior,
21
22 electrochemical impedance spectroscopy (EIS) measurements with Bode phase plots and
23
24 Nyquist plots were conducted and plotted, respectively (Figure 3d and Supporting
25
26 Information Figures S5). All the Nyquist plots for the NiMoO₄ electrodes show that the
27
28 charge transfer resistances (R_{ct}), recorded from the diameters of the semicircle, are very low.
29
30 This outcome demonstrates that the NiMoO₄ electrodes grown directly on the Ni foam
31
32 current collector have nearly equal electrolyte resistance and superior charge transfer, which
33
34 minimizes interfacial resistance and facilitates charge transfer at the interface between the
35
36 current collector and electrode material. Furthermore, the linear part in the plot of the HAR-
37
38 NiMoO₄ sample in the low frequency region (Warburg impedance) is significantly steeper
39
40 than that for the MAR- and LAR-NiMoO₄ samples, suggesting that the HAR-NiMoO₄ has the
41
42 fastest ion diffusion and electrolyte access to the surface, which is consistent with the results
43
44 of the capacitance rate retention in Figure 3c.³¹
45
46

47
48 Figure 3d shows the Bode phase plots for the NiMoO₄ electrodes with the different
49
50 relaxation time constant (τ_0). A relaxation time constant can be calculated from the x-axis
51
52 frequency when the curve reaches -45° on the Bode plot. The relaxation time constant is an
53
54 important parameter so as to compare between capacitive and resistive behaviors of a
55
56 supercapacitors dependence on frequency.³² As shown in Figure 3d, the HAR-NiMoO₄
57
58
59

60

1
2
3
4 sample exhibits the fastest relaxation time constant ($\tau_0 = 1.73$ s) compared to that of the
5
6 MAR- and LAR-NiMoO₄ samples which are 3.49 s and 6.87 s, respectively. Here, it should
7
8 be noted that the fast relaxation time constant implies that the HAR-NiMoO₄ sample can
9
10 introduce a fast capacitive response. It can be clearly observed that the phase angle of HAR-
11
12 NiMoO₄ at a low frequency of $f = 0.01$ Hz was about -81° , which is the closest value to -90° ,
13
14 implying ideal capacitor behavior because of its low electrolyte resistance and fast electrolyte
15
16 intercalation.³³ Overall, the electrochemical relationships for the NiMoO₄ electrodes with the
17
18 different 1-D morphologies are illustrated in Figure 3e. The HAR-NiMoO₄ electrode
19
20 nanostructure not only provides the largest contact sites, which lead to a large density of
21
22 electrolyte ions near the surface, but also facilitates more efficient electrochemical reactions
23
24 through the highest degree of ion diffusion towards the inside of the electrode. Additionally,
25
26 its high electrical conductivity and low surface resistance enable fast charge transfer through
27
28 a pseudocapacitor system. Such behavior is strongly correlated to the high capacitance, fast
29
30 retention rate and charge transfer mechanism of the HAR-NiMoO₄ electrode.

31
32
33 To further demonstrate the potential of the NiMoO₄ electrode for practical
34
35 supercapacitor applications, an asymmetric supercapacitor (ASC) was fabricated using the
36
37 HAR-NiMoO₄ material as the cathode and active carbon (AC) as the anode. Figure 4a shows
38
39 the comparative CV plots of the individual positive and negative electrodes in the ASC at a
40
41 scan rate of 5 mV s^{-1} . The AC exhibits a typical rectangular electric double-layer capacitor
42
43 (EDLC) performance within the range of -1.0 to 0.0 V, and the HAR-NiMoO₄ shows
44
45 pseudocapacitance behavior within the range of 0.0 to 0.6 V. Therefore, the AC//HAR-
46
47 NiMoO₄ ASC can operate from 0 to 1.6 V with a wide operating potential. To design the ASC
48
49 with the ideal capacitance, the mass of the individual electrodes is optimized according to the
50
51 following formula.³⁴
52
53
54
55
56
57
58
59
60

$$Q_+ = Q_- \rightarrow \frac{m_+}{m_-} = \frac{C_- * \Delta V_-}{C_+ * \Delta V_+}$$

where C_- and C_+ are the calculated capacitance of the negative and positive electrodes, respectively, and ΔV_- and ΔV_+ are the operating potential windows of the negative and positive electrodes, respectively. Therefore, on the basis of C_- and the potential window of the AC electrode, the optimum loading ratio of HAR-NiMoO₄ to AC is 1:3.126.

Figure 4b shows CV curves of the ASC device at various scan rates, ranging from 50 to 5 mV s⁻¹. It can be seen that the shape of the CV curves involves both EDLC and pseudocapacitance contribution from the rectangular shape and the redox humps. The CV curves of the ASC are found to maintain a similar profile with increasing scan rates, indicating good capacitive behavior. As shown in the inset of Figure 4c, galvanostatic charge/discharge curves for the ASC were measured at current densities from 1 to 20 A g⁻¹ in a potential window of 0 to 1.6 V. In addition, the calculated capacitance as a function of the discharge current density is plotted (Supporting Information Figure S4). This device shows good electrochemical performance and the specific capacitance was calculated to be 114.4 F g⁻¹ at a current density of 1 A g⁻¹. Furthermore, the ASC exhibits good cycling stability, retaining up to 82.2 % after 2000 charge-discharge cycles at a current density of 5 A g⁻¹ (Figure 4c). To compare the energy density and power density with other reported ASCs, the Ragone plots of the AC//HAR-NiMoO₄ ASC were derived in Figure 4d, showing that an energy density of 40.6 Wh kg⁻¹ and a power density of 16 kW kg⁻¹ can be achieved. Clearly, the device performance compares favorably with other asymmetric supercapacitors.³⁵⁻⁴¹ It is shown that the HAR-NiMoO₄ exhibits a high specific capacitance and high ionic and electric transfer rates, along with good electrochemical behavior because: (1) the direct growth of the 1-D NiMoO₄ sample on the Ni foam provides good electron transfer due to the low contact resistance between the active material and the current collector; (2) the highly ordered 1-D

1
2
3
4 nanostructure with a high aspect ratio not only leads to a large diffusion coefficient, but also
5
6 results in a large contact area and (3) this gives rises to numerous ion diffusion channels,
7
8 thereby inducing a high rate retention response.
9

10 11 12 13 **CONCLUSION**

14
15 In summary, we have demonstrated that 1-D NiMoO₄ electrodes grown directly onto
16
17 a nickel foam have been successfully prepared via a simple supersaturation-controlled
18
19 hydrothermal process. The resulting 1-D NiMoO₄ electrodes, each with a different aspect
20
21 ratio, can be predictively adjusted by changing the supersaturation states and consequently
22
23 the driving force for nucleation and crystal growth. Moreover, electrochemical measurements
24
25 indicate that the HAR-NiMoO₄ electrode exhibits the best specific capacitance and superior
26
27 rate retention performance such as a large specific capacitance of 1335 F g⁻¹ at a current
28
29 density of 1 A g⁻¹ with a good rate retention of 66.1 %. We also showed that the AC//HAR-
30
31 NiMoO₄ ASC with a wide potential window of 1.6 V exhibits the energy density of 40.7 Wh
32
33 kg⁻¹ and the power density of 16 kW kg⁻¹ compared to other reported pseudo-capacitive
34
35 ASCs. Furthermore, we successfully demonstrated that the HAR-NiMoO₄ electrode provides
36
37 a better contact surface area, ion diffusion behavior and enhanced charge transfer kinetics
38
39 based on the hierarchical 1-D nanostructure. This deterministic and predictive synthesis
40
41 method, which is controlled by adjusting the solubility in a hydrothermal approach, is a
42
43 promising technique to producing highly efficient pseudo-capacitive electrodes with 1-D
44
45 nanostructures. Such electrodes can easily promote dynamic electrochemical kinetics,
46
47 including high Faradaic capacitance, high retention and fast charge transfer rate for practical
48
49 pseudocapacitor applications.
50
51
52
53
54
55
56
57
58
59
60

1
2
3
4 **Acknowledgments**
5

6 This work was supported by the Industrial Fundamental Technology Development Program
7
8 from the Ministry of Trade, Industry and Energy (MOTIE) of Korea [10052745,
9
10 Development of nano-sized (100nm) manganese ceramic material for high voltage pseudo-
11 capacitor]; International Collaborative Energy Technology R&D Program of the Korea
12
13 Institute of Energy Technology Evaluation and Planning (KETEP) from Ministry of Trade,
14
15 Industry & Energy of Korea [20138520030800]. Also, SMM acknowledges The Royal
16
17
18
19
20 Society for financial support.
21
22
23
24
25
26
27
28
29
30
31
32
33
34
35
36
37
38
39
40
41
42
43
44
45
46
47
48
49
50
51
52
53
54
55
56
57
58
59
60

1
2
3
4 **Figure captions**
5

6 **Figure 1.** Illustration of the nanostructures and crystal growth mechanisms of (a) HAR-, (b)
7 MAR- and (c) LAR-NiMoO₄ 1-D nanostructures with different aspect ratios. 1-D
8 nanostructures are systematically controlled by using different supersaturation states during
9 the growth phase. (d-f) SEM images of the HAR-, MAR- and LAR-NiMoO₄ 1-D
10 nanostructures. Inset images show the corresponding TEM images of the three different 1-D
11 nanostructures.
12
13
14
15
16
17
18

19 **Figure 2.** (a) XRD patterns of the as-prepared NiMoO₄ nanostructures. Asterisks show XRD
20 patterns of the nickel foam. (b) Calculated BET specific surface areas of the as-prepared
21 NiMoO₄ nanostructures. (c) Ni 2p and (d) Mo 3d XPS spectra of the as-prepared NiMoO₄
22 nanostructures. Inset: images show that Ni cations in the octahedral site and Mo cations in the
23 tetrahedral site contribute to the electrochemical reaction and stability, respectively.
24
25
26
27
28
29
30

31 **Figure 3.** (a) CV curves for HAR-, MAR-, and LAR-NiMoO₄ electrodes at a scan rate of 5
32 mV s⁻¹ in 1.0 M KOH. The inset shows the redox potential gap (ΔE_p) for the different
33 NiMoO₄ samples. (b) Cathodic peak current density as a function of the square root of the
34 scan rate for the three different samples. (c) Comparison of the capacitance retention and (d)
35 Bode phase plots for the HAR-, MAR-, and LAR-NiMoO₄ samples. (e) Illustration of the
36 relationship between the tailored NiMoO₄ nanostructures and the pseudo-capacitive behavior
37 including electrolyte ion diffusion and electron transfer dynamics.
38
39
40
41
42
43
44
45
46

47 **Figure 4.** (a) Comparative CV curves of the HAR-NiMoO₄ and AC electrodes at 5 mV s⁻¹ in
48 a three electrode system. (b) CV curves and (c) Cycling stability of the AC//HAR-NiMoO₄
49 ASC. The inset image shows galvanostatic charge-discharge curves of the ASC. (d) Ragone
50 plot of the AC//HAR-NiMoO₄ ASC in comparison with other reported ASCs.
51
52
53
54
55
56
57
58
59
60

References

- 1 Wang, G.; Zhang, L.; Zhang, J. A Review of Electrode Materials for Electrochemical Supercapacitors. *Chem. Soc. Rev.* **2011**, *41*, 797–828.
- 2 Yan, J.; Wang, Q.; Wei, T.; Fan, Z. Recent Advances in Design and Fabrication of Electrochemical Supercapacitors with High Energy Densities. *Adv. Energy Mater.* **2014**, *4*, 1300816.
- 3 Simon, P.; Gogotsi, Y. Materials for Electrochemical Capacitors. *Nature Mater.* **2008**, *7*, 845–854.
- 4 Augustyn, V.; Simon, P.; Dunn, B. Pseudocapacitive Oxide Materials for High-Rate Electrochemical Energy Storage. *Energy Environ. Sci.* **2014**, *7*, 1597–1614.
- 5 Fisher, R.; Watt, M.; Ready, W. Functionalized Carbon Nanotube Supercapacitor Electrodes: A Review on Pseudocapacitive Materials. *ECS J. Solid State Sci. Technol.* **2013**, *2*, M3170–M3177.
- 6 Chou, J.-C.; Chen, Y.-L.; Yang, M.-H.; Chen, Y.-Z.; Lai, C.-C.; Chiu, H.-T.; Lee, C.-Y.; Chueh, Y.-L.; Gan, J.-Y. RuO₂/MnO₂ Core-shell Nanorods for Supercapacitors. *J. Mater. Chem. A* **2013**, *1*, 8753–8758.
- 7 Zhu, Y.; Cao, C.; Tao, S.; Chu, W.; Wu, Z.; Li, Y. Ultrathin Nickel Hydroxide and Oxide Nanosheets: Synthesis, Characterizations and Excellent Supercapacitor Performances. *Sci. Rep.* **2014**, *4*, 5787.
- 8 Liu, W.; Li, X.; Zhu, M.; He, X. High-Performance All-Solid State Asymmetric Supercapacitor Based on Co₃O₄ Nanowires and Carbon Aerogel. *J. Power Sources* **2015**, *282*, 179–186.
- 9 Ma, X.; Kolla, P.; Zhao, Y.; Smirnova, A.; Fong, H. Electrospun Lignin-Derived Carbon Nanofiber Mats Surface-Decorated with MnO₂ Nanowhiskers as Binder-Free Supercapacitor Electrodes with High Performance. *J. Power Sources* **2016**, *325*, 541–

- 1
2
3
4 548.
5
6
7
8
9
10
11
12
13
14
15
16
17
18
19
20
21
22
23
24
25
26
27
28
29
30
31
32
33
34
35
36
37
38
39
40
41
42
43
44
45
46
47
48
49
50
51
52
53
54
55
56
57
58
59
60
- 10 Wu, Z.; Zhu, Y.; Ji, X. NiCo₂O₄-Based Materials for Electrochemical Supercapacitors. *J. Mater. Chem. A* **2014**, *2*, 14759–14772.
- 11 Li, L.; Peng, S.; Cheah, Y.; Teh, P.; Wang, J.; Wee, G.; Ko, Y.; Wong, C.; Srinivasan, M. Electrospun Porous NiCo₂O₄ Nanotubes as Advanced Electrodes for Electrochemical Capacitors. *Chem. - A Euro. J.* **2013**, *19*, 5892–5898.
- 12 Hu, J.; Li, M.; Lv, F.; Yang, M.; Tao, P.; Tang, Y.; Liu, H.; Lu, Z. Heterogeneous NiCo₂O₄@polypyrrole Core/sheath Nanowire Arrays on Ni Foam for High Performance Supercapacitors. *J. Power Sources* **2015**, *294*, 120–127.
- 13 Pendashteh, A.; Rahmanifar, M.; Kaner, R.; Mousavi, M. Facile Synthesis of Nanostructured CuCo₂O₄ as a Novel Electrode Material for High-Rate Supercapacitors. *Chem. Comm.* **2013**, *50*, 1972–1975.
- 14 Peng, S.; Li, L.; Hu, Y.; Srinivasan, M.; Cheng, F.; Chen, J.; Ramakrishna, S. Fabrication of Spinel One-Dimensional Architectures by Single-Spinneret Electrospinning for Energy Storage Applications. *ACS Nano* **2015**, *9*, 1945–1954.
- 15 Li, L.; Peng, S.; Wu, H.; Yu, L.; Madhavi, S.; Lou, X. A Flexible Quasi-Solid-State Asymmetric Electrochemical Capacitor Based on Hierarchical Porous V₂O₅ Nanosheets on Carbon Nanofibers. *Adv. Energy Mater.* **2015**, *5*, 1500753.
- 16 Xia, X.; Lei, W.; Hao, Q.; Wang, W.; Wang, X. One-Step Synthesis of CoMoO₄/graphene Composites with Enhanced Electrochemical Properties for Supercapacitors. *Electrochim. Acta* **2013**, *99*, 253–261.
- 17 Xiao, K.; Xia, L.; Liu, G.; Wang, S.; Ding, L.-X.; Wang, H. Honeycomb-like NiMoO₄ Ultrathin Nanosheet Arrays for High-Performance Electrochemical Energy Storage. *J. Mater. Chem. A* **2015**, *3*, 6128–6135.
- 18 Wang, S.; Sun, S.; Li, S.; Gong, F.; Li, Y.; Wu, Q.; Song, P.; Fang, S.; Wang, P. Time

- 1
2
3
4 and Temperature Dependent Multiple Hierarchical NiCo₂O₄ for High-Performance
5 Supercapacitors. *Dalton Tran.* **2016**, *45*, 7469–7475.
6
7
8
9 19 Zhang, G.; Lou, X. Controlled Growth of NiCo₂O₄ Nanorods and Ultrathin Nanosheets
10 on Carbon Nanofibers for High-Performance Supercapacitors. *Sci Rep.* **2013**, *3*, 1470.
11
12
13 20 Xiang, N.; Ni, Y.; Ma, X. Shape-Controlled Synthesis of NiCo₂O₄ Microstructures and
14 Their Application in Supercapacitors. *Chem. Asian J.* **2015**, *10*, 1972–1978.
15
16
17 21 Zhu, T.; Koo, E.; Ho, G. Shaped-Controlled Synthesis of Porous NiCo₂O₄ with 1-3
18 Dimensional Hierarchical Nanostructures for High-Performance Supercapacitors. *RSC*
19 *Adv.* **2014**, *5*, 1697–1704.
20
21
22
23 22 Chithambararaj; Yogamalar, R.; Bose, C. Hydrothermally Synthesized H-MoO₃ and A-
24 MoO₃ Nanocrystals: New Findings on Crystal-Structure-Dependent Charge
25 Transport. *Cryst. Growth. Des.* **2016**, *16*, 1984–1995.
26
27
28
29 23 Huang, Z.; Zhang, Z.; Qi, X.; Ren, X.; Xu, G.; Wan, P.; Sun, X.; Zhang, H. Wall-like
30 Hierarchical Metal Oxide Nanosheet Arrays Grown on Carbon Cloth for Excellent
31 Supercapacitor Electrodes. *Nanoscale* **2016**, *8*, 13273–13279.
32
33
34
35 24 Yan, J.; Fan, Z.; Sun, W.; Ning, G.; Wei, T.; Zhang, Q.; Zhang, R.; Zhi, L.; Wei, F.
36 Advanced Asymmetric Supercapacitors Based on Ni(OH)₂/Graphene and Porous
37 Graphene Electrodes with High Energy Density. *Adv. Funct. Mater.* **2012**, *22*, 2632–
38 2641.
39
40
41
42 25 Ghosh, D.; Giri, S.; Das, C. Synthesis, Characterization and Electrochemical
43 Performance of Graphene Decorated with 1D NiMoO₄·nH₂O Nanorods.
44 *Nanoscale* **2013**, *5*, 10428–10437.
45
46
47
48
49 26 Pang, H.; Wei, C.; Li, X.; Li, G.; Ma, Y.; Li, S.; Chen, J.; Zhang, J. Microwave-Assisted
50 Synthesis of NiS₂ Nanostructures for Supercapacitors and Cocatalytic Enhancing
51 Photocatalytic H₂ Production. *Sci. Rep.* **2014**, *4*, 3577.
52
53
54
55
56
57
58
59
60

- 1
2
3
4 27 Senthilkumar, B.; Sankar, K.; Selvan, R.; Danielle, M.; Manickam, M. Nano A-NiMoO₄
5 as a New Electrode for Electrochemical Supercapacitors. *RSC Adv.* **2012**, *3*, 352–357.
6
7
8 28 Mai, L.; Li, H.; Zhao, Y.; Xu, L.; Xu, X.; Luo, Y.; Zhang, Z.; Ke, W.; Niu, C.; Zhang, Q.
9
10 Fast Ionic Diffusion-Enabled Nanoflake Electrode by Spontaneous Electrochemical
11 Pre-Intercalation for High-Performance Supercapacitor. *Sci. Rep.* **2013**, *3*, 1718.
12
13 29 Xu, P.; Liu, J.; Yan, P.; Miao, C.; Ye, K.; Cheng, K.; Yin, J.; Cao, D.; Li, K.; Wang, G.
14 Preparation of Porous Cadmium Sulphide on Nickel Foam: A Novel Electrode Material
15 with Excellent Supercapacitor Performance. *J. Mater. Chem. A* **2016**, *4*, 4920–4928.
16
17
18 30 Liu, S.; Hui; Hui Flower-like Copper Cobaltite Nanosheets on Graphite Paper as High-
19 Performance Supercapacitor Electrodes and Enzymeless Glucose Sensors. *ACS Appl.*
20 *Mater. Interfaces* **2016**, *8*, 3258–3267.
21
22 31 Pendashteh, A.; Moosavifard, S.; Rahmanifar, M.; Wang, Y.; El-Kady, M.; Kaner, R.;
23 Mousavi, M. Highly Ordered Mesoporous CuCo₂O₄ Nanowires, a Promising Solution
24 for High-Performance Supercapacitors. *Chem. Mater.* **2015**, *27*, 3919–3926.
25
26 32 Pan, X.; Ren, G.; Hoque, M. N. F.; Bayne S.; Zhu, K.; Fan, Z. Fast Supercapacitors
27 Based on Graphene-Bridged V₂O₃/VO_x Core–Shell Nanostructure Electrodes with a
28 Power Density of 1 MW kg⁻¹. *Adv. Mater. Inter.* **2014**, *1*, 1400398.
29
30
31 33 Yuan, L.; Lu, X.-H.; Xiao, X.; Zhai, T.; Dai, J.; Zhang, F.; Hu, B.; Wang, X.; Gong, L.;
32 Chen, J.; Hu, C.; Tong, Y.; Zhou, J.; Wang, Z. L. Flexible Solid-State Supercapacitors
33 Based on Carbon Nanoparticles/MnO₂ Nanorods Hybrid Structure. *ACS Nano* **2012**, *6*,
34 656–661.
35
36
37 34 Ren, X.; Guo, C.; Xu, L.; Li, T.; Hou, L.; Wei, Y. Facile Synthesis of Hierarchical
38 Mesoporous Honeycomb-like NiO for Aqueous Asymmetric Supercapacitors. *ACS*
39 *Appl. Mater. Interfaces* **2015**, *7*, 19930–19940.
40
41
42 35 Li, X.; Jiang, L.; Zhou, C.; Liu, J.; Zeng, H. Integrating Large Specific Surface Area
43
44
45
46
47
48
49
50
51
52
53
54
55
56
57
58
59
60

- 1
2
3
4 and High Conductivity in Hydrogenated NiCo₂O₄ Double-Shell Hollow Spheres to
5 Improve Supercapacitors. *NPG Asia Mater.* **2015**, 7, e165.
6
7
8
9 36 Cheng, D.; Yang, Y.; Xie, J.; Fang, C.; Zhang, G.; Xiong, J. Hierarchical
10 NiCo₂O₄@NiMoO₄ Core-shell Hybrid Nanowire/nanosheet Arrays for High-
11 Performance Pseudocapacitors. *J. Mater. Chem. A* **2015**, 3, 14348–14357.
12
13
14 37 Wang, X.; Liu, W. S.; Lu, X.; Lee, P. S. Dodecyl Sulfate-Induced Fast Faradic Process
15 in Nickel Cobalt Oxide-reduced Graphite Oxide Composite Material and Its
16 Application for Asymmetric Supercapacitor Device. *J. Mater. Chem.* **2012**, 22, 23114–
17 23119.
18
19
20 38 Yang, J.; Li, G.; Pan, Z.; Liu, M.; Hou, Y.; Xu, Y.; Deng, H.; Sheng, L.; Zhao, X.; Qiu,
21 Y.; Zhang, Y. All-Solid-State High-Energy Asymmetric Supercapacitors Enabled by
22 Three-Dimensional Mixed-Valent MnO_x Nanospike and Graphene Electrodes. *ACS*
23 *Appl. Mater. Interfaces* **2015**, 7, 22172–22180.
24
25
26 39 Senthilkumar, B.; Meyrick, D.; Lee, Y.-S.; Selvan, R. Synthesis and Improved
27 Electrochemical Performances of Nano β-NiMoO₄-CoMoO₄·xH₂O Composites for
28 Asymmetric Supercapacitors. *RSC Adv.* **2013**, 3, 16542–16548.
29
30
31 40 Ma, X.-J.; Kong, L.-B.; Zhang, W.-B.; Liu, M.-C.; Luo, Y.-C.; Kang, L. Design and
32 Synthesis of 3D Co₃O₄@MMoO₄ (M=Ni, Co) Nanocomposites as High-Performance
33 Supercapacitor Electrodes. *Electrochim. Acta* **2014**, 130, 660–669.
34
35
36 41 Xiao, K.; Xia, L.; Liu, G.; Wang, S.; Ding, L.-X.; Wang, H. Honeycomb-like NiMoO₄
37 Ultrathin Nanosheet Arrays for High-Performance Electrochemical Energy Storage. *J.*
38 *Mater. Chem. A* **2015**, 3, 6128-6135.
39
40
41
42
43
44
45
46
47
48
49
50
51
52
53
54
55
56
57
58
59
60

1
2
3
4
5
6
7
8
9
10
11
12
13
14
15
16
17
18
19
20
21
22
23
24
25
26
27
28
29
30
31
32
33
34
35
36
37
38
39
40
41
42
43
44
45
46
47
48
49
50
51
52
53
54
55
56
57
58
59
60

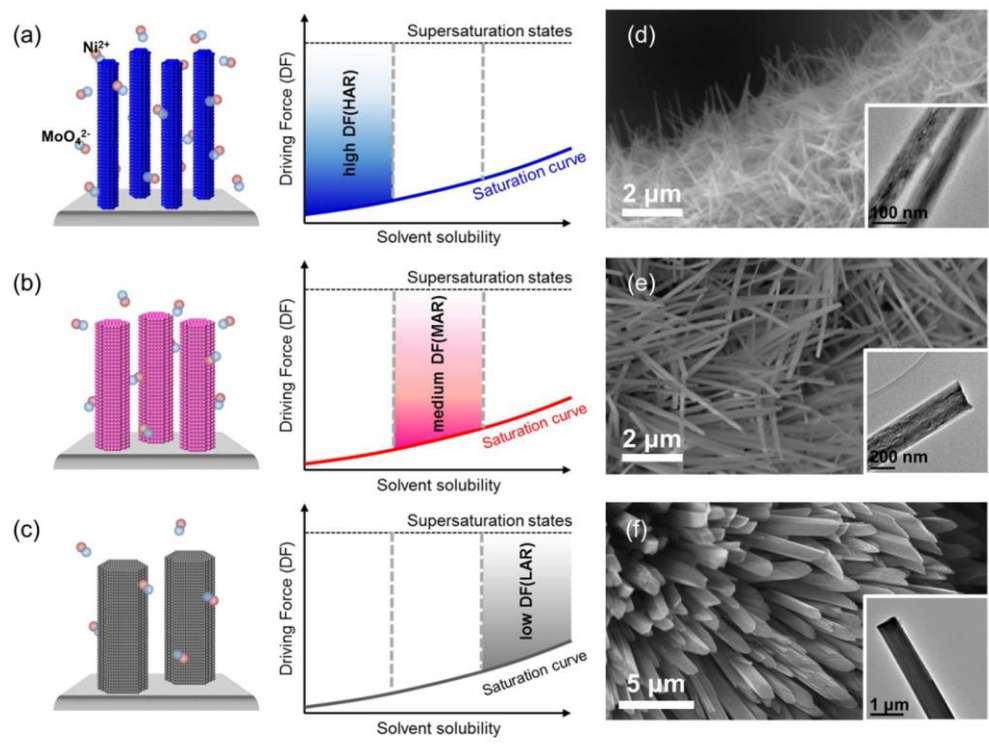


Figure 1. Hong *et. al.*

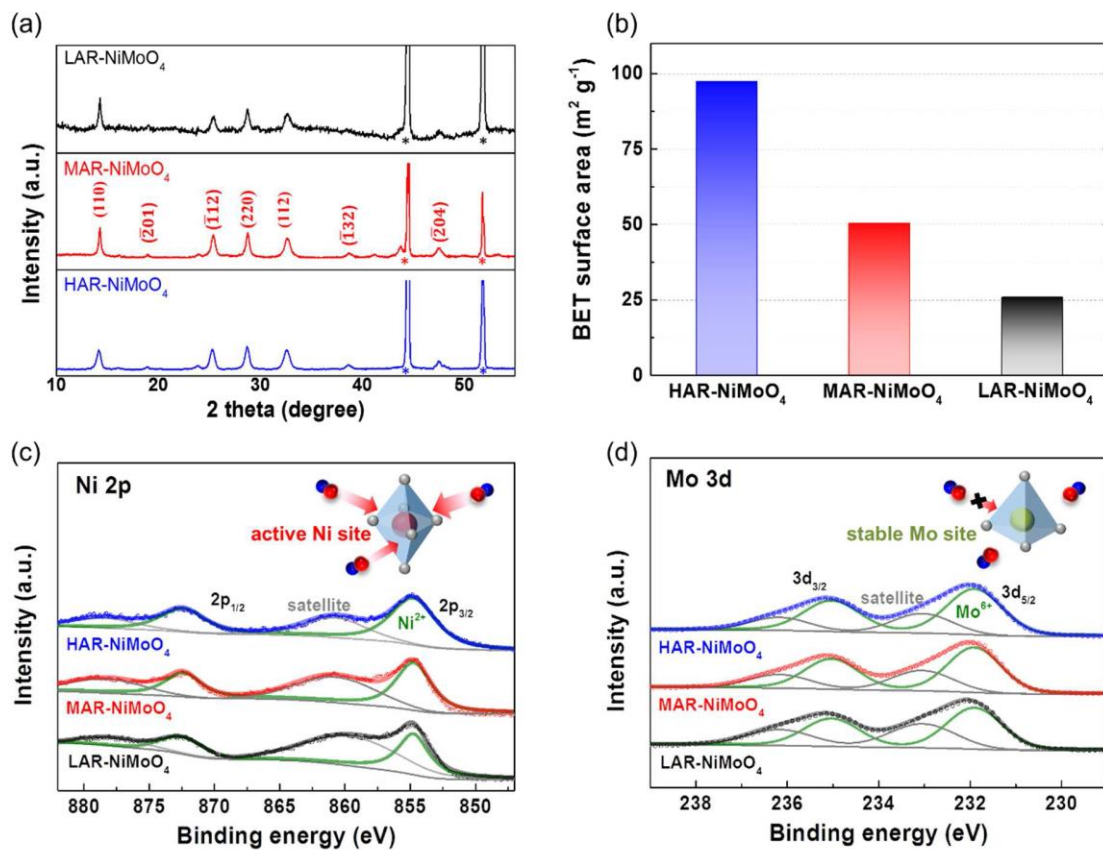


Figure 2. Hong *et. al.*

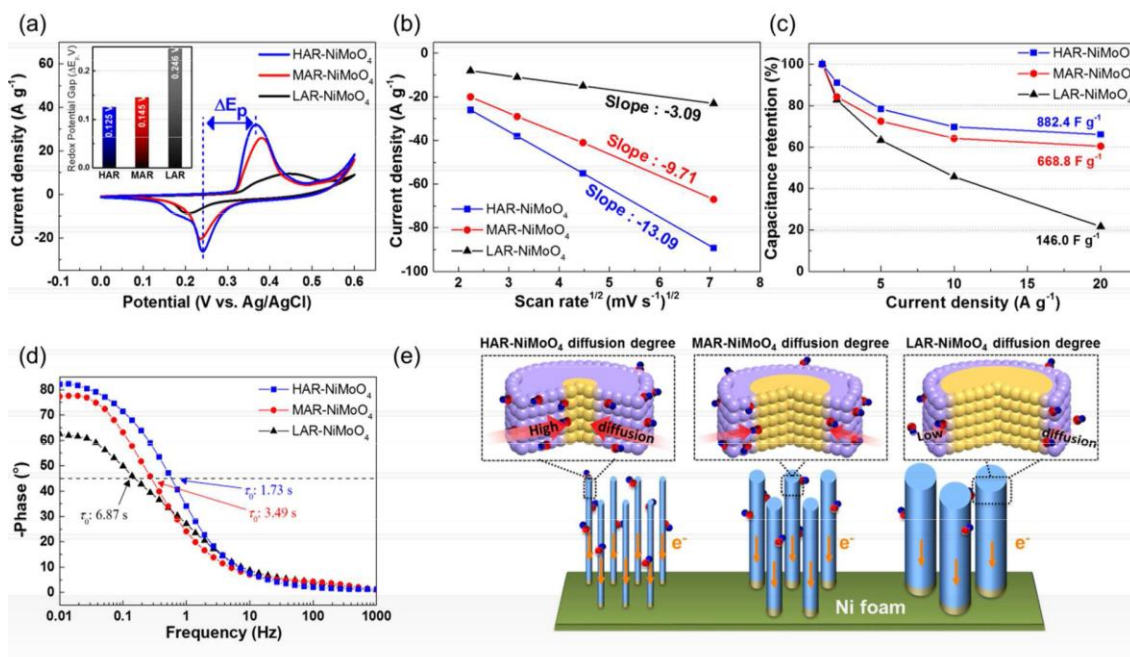


Figure 3. Hong *et. al.*

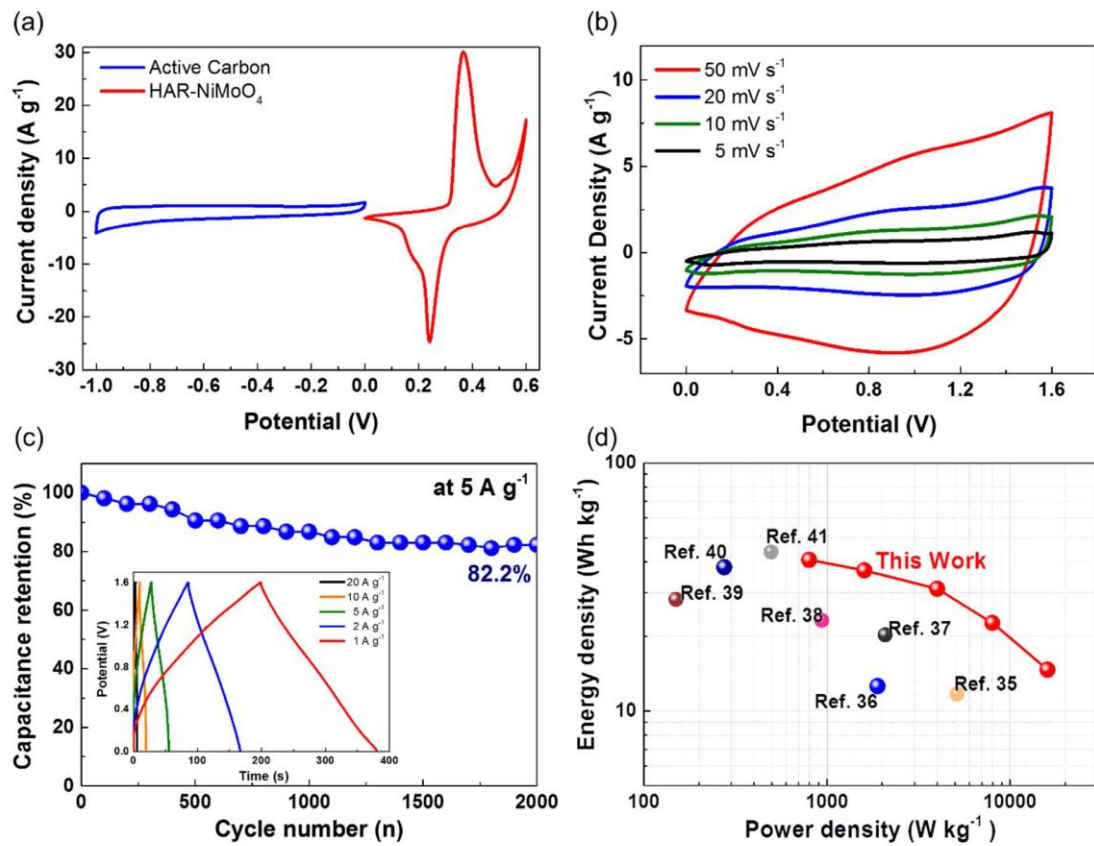


Figure 4. J. Hong *et. al.*

Table of Contents

